

# Differentiable Graph Neural Network Simulator for the Back-Analysis of Post-Liquefaction Residual Strength from Flow Failure Runout

Yongjin Choi<sup>a</sup>, Jorge Macedo<sup>a</sup>

<sup>a</sup>*School of Civil and Environmental Engineering, Atlanta, Georgia Institute of Technology, Atlanta, 30332, GA, USA*

---

## Abstract

This study introduces Differentiable Graph Neural Network Simulators (Diff-GNS) as a physics-informed and automated framework for estimating post-liquefaction residual strengths ( $S_r$ ). Traditional approaches to estimate  $S_r$  rely on simplified physics, manual iterations, and assumptions about runout development. Diff-GNS overcomes these limitations by integrating a Graph Neural Network Simulator (GNS) that simulates granular flows, with gradient-based optimization through automatic differentiation. GNS accelerates forward runout simulations that are otherwise computationally intensive with conventional numerical methods, while gradient-based optimization automates the inversion to back-calculate  $S_r$ . The GNS is trained on simulations with the material point method on geometries informed by case-history runout failures, enabling focused learning of realistic runout mechanisms and the ability to simulate slopes across small and large scales. The Diff-GNS framework is validated using two well-documented liquefaction-induced flow failure case histories: the Lower San Fernando dam and La Marquesa dam. In the two cases, the inferred  $S_r$  agrees closely with published estimates and reproduces physically consistent runout behaviors. The framework also has the ability to jointly infer multiple interacting parameters, extending beyond single-parameter back-analyses. By embedding the physics of runout processes, minimizing manual intervention, and accelerating the inversion process to estimate  $S_r$ , Diff-GNS provides an efficient, reproducible, and physically grounded approach for geotechnical analysis of liquefaction-induced flow failures.

*Keywords:* Runout, Post-liquefaction residual strength, Graph neural network simulator, Differentiable simulation, Inverse analysis,

---

## 1. Introduction

Over the past decades, methods for estimating the post-liquefaction residual shear strength ( $S_r$ ) and evaluating post-failure runout in slope systems have evolved. Initial reliance on laboratory testing to estimate  $S_r$  faced challenges in replicating in-situ field conditions, particularly the effects of void redistribution and sample disturbance (Poulos et al., 1985; Castro et al., 1992). These difficulties steered the focus toward the back-analysis of full-scale field case histories. Back analyses typically use field observation data, i.e., failure geometry and runout characteristics, to infer the operational shear strengths of the soil mass that can explain the observed failure runout. Early back-analysis methods (Seed, 1987; Seed and Harder Jr, 1990) were based on simple limit equilibrium principles applied to the static geometries of the slope before and after failure. However, static analyses neglect the kinetic energy and momentum carried by the sliding mass during failure, known as momentum effects (Olson and Stark, 2002).

Previous efforts to consider momentum effects in back-analysis include the kinetics method (Olson, 2001; Olson and Stark, 2002), the zero inertial factor (ZIF) method (Kramer and Wang, 2015), and the incremental momentum method (IMM) (Weber, 2015). These methods have been used to evaluate well-known case histories; however, each method faces limitations. The kinetics method, for example, simplifies the failure mass to a rigid block with a pre-assumed sliding path. The ZIF method relies on an intermediate sliding mass at an inferred instance of zero acceleration, with several assumptions for its definition. The IMM involves manually constructing a sequence of kinematically feasible cross-sections, making the analysis subject to a range of plausible interpretations and time-consuming.

Addressing the highlighted shortcomings calls for a paradigm shift to assess runout flow failures and  $S_r$ , from manual, interpretive techniques that can involve significant judgment, toward a more automated, physics-consistent, and computationally efficient approach. Numerical techniques capable of simulating large deformations, such as the Material Point Method (MPM), can offer a more physically rigorous foundation (Macedo et al., 2024a; De Vaucorbeil et al., 2020). However, they are not computationally efficient, runtimes can vary from hours to days (Abram et al., 2022; Ceccato et al., 2024), limiting their practical application. This computational burden becomes

especially prohibitive in back analyses that seek to estimate  $S_r$ , because they would require repeated forward simulations to iteratively refine strength parameters.

Addressing the limitations of simplified methods and the high computational cost of numerical approaches such as MPM, this study introduces a computationally efficient framework for back-calculating  $S_r$  while maintaining a physics-informed runout progression during failure, leveraging the Graph Neural Network simulator (GNS) concept developed by DeepMind (Sanchez-Gonzalez et al., 2020). The framework couples a trained GNS in this study with gradient-based optimization via reverse-mode automatic differentiation (AD) (Baydin et al., 2018), yielding a Differentiable Graph Neural Network Simulator (Diff-GNS) capable of inferring material parameters efficiently. Previous GNS applications (Choi and Kumar, 2024a, 2023; Zhao et al., 2025) have demonstrated the GNS potential as an efficient surrogate for granular flow simulations, but remained largely proof-of-concept, limited to small domains (1-2 m), idealized cube-shaped masses, and homogeneous materials characterized only by friction angle. The only study we know that extended GNS to realistic slope systems (Choi et al. (2025)) provided encouraging results but relied on training with randomly generated geometries, not directly related to slope case history failures. In contrast, this study designs the training datasets informed by case histories and develops distinct models for small and large-scale slopes, enabling representation of systems spanning tens to hundreds of meters, a capability not included in earlier efforts. These advances move GNS from conceptual validation toward a practical tool for estimating  $S_r$  and simulating runout in slope systems. We evaluate the Diff-GNS's performance in back-analyzing  $S_r$  and simulating runout dynamics, considering two liquefaction flow failures: the Lower San Fernando dam and the La Marquesa dam. To our knowledge, this is the first assessment of Diff-GNN for real-world runout case histories.

The manuscript is organized as follows: Section 2 reviews traditional  $S_r$  estimation methods and their limitations. Section 3 presents the theoretical basis of the Diff-GNS framework and its advantages. Section 4 describes the training of the GNS implemented in this study. Section 5 evaluates the trained GNS's performance in estimating  $S_r$  and simulating realistic runout for selected case histories.

## 2. Existing methods to back-calculate residual strength

**Kinetics Method.** The kinetics method (Olson, 2001; Olson and Stark, 2002), illustrated in Figure 1a, applies dynamic equilibrium ( $\sum F = m \cdot a$ ) to back-calculate  $S_r$ , explicitly accounting for momentum effects. The failed mass is idealized as a rigid body translating downslope, with its center-of-gravity (CG) path approximated by a third-order polynomial. The slope of this curve defines the driving force ( $W \sin \theta$ ), while resistance equals  $S_r L$ . Incremental time-stepping analysis updates acceleration, velocity, and displacement to track the rigid body's motion.  $S_r$  is iteratively adjusted until the final computed CG position matches field observations. The method is sensitive to the assumed CG path and relies on rigid-body idealized motion.

**Zero Inertial Factor (ZIF) Method.** The ZIF method (Kramer and Wang, 2015), illustrated in Figure 1b, provides a static approach to implicitly account for the momentum effect by identifying the motion stage where acceleration is zero and forces balance. ZIF is defined as the fraction of total displacement at this stage, typically assumed to be 40-50%, or estimated from the kinetics method. To build the ZIF geometry (gray line in Figure 1b), points from the pre-failure cross-section (black dots) are shifted toward the post-failure geometry according to the ZIF value, and the displaced points ( $\times$  markers) define ZIF. Static limit-equilibrium analysis is then performed on this geometry to back-calculate  $S_r$  with a safety factor of 1.0. The method avoids dynamic modeling but depends heavily on engineering judgment to define the ZIF geometry, which may require iteration and limit reproducibility.

**Incremental Momentum Method (IMM).** IMM (Weber, 2015) addresses limitations of the kinetics and ZIF methods by reconstructing a sequence of intermediate geometries that progressively track the slope from its initial to final state. At each stage, driving and resisting forces are calculated, and Newton's second law is applied incrementally to update acceleration, velocity, and displacement until the modeled runout matches observations. This stepwise approach captures evolving geometries, accommodates progressive failure, and avoids curve-fitting assumptions such as polynomial CG paths. However, it is labor-intensive and relies heavily on engineering judgment to define intermediate physically plausible stages, making results dependent on the analyst.

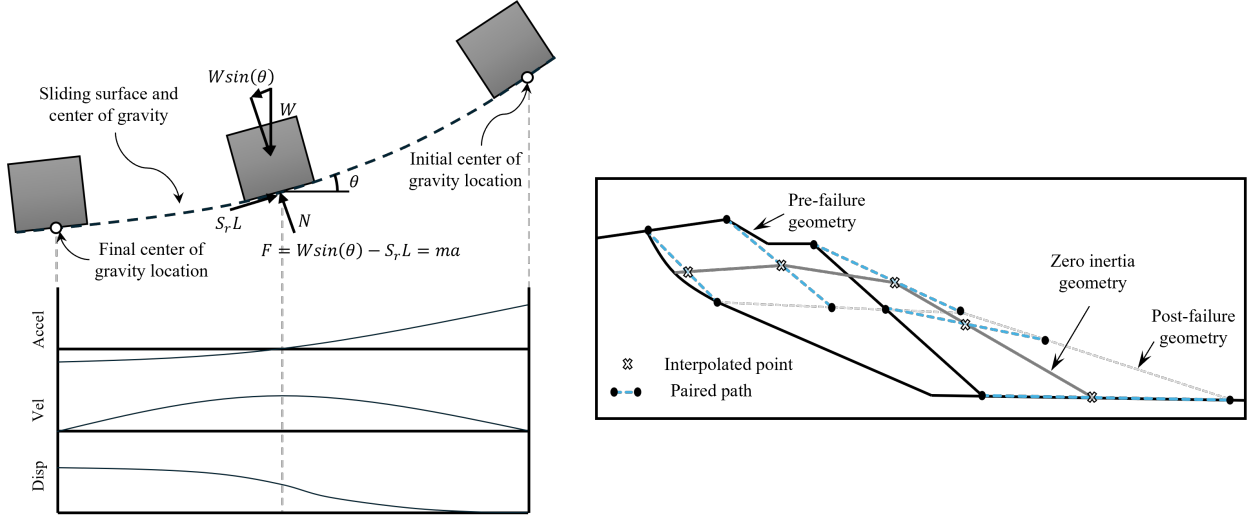


Figure 1: Conceptual illustration of (a) the Kinetics method (after Olson (2001)) and (b) the Zero Inertial Factor (ZIF) method (after Kramer and Wang (2015)) for back-analysis of post-liquefaction residual strength  $S_r$ .

### 3. Differentiable graph neural network simulator-based framework

#### 3.1. Graph Neural Network Simulator (GNS) for Granular Flow

GNS can be used as a generalizable surrogate for conventional numerical solvers that simulate granular flows. Below, we briefly introduce the GNS architecture using Figure 2. For further details, see the original works from Sanchez-Gonzalez et al. (2020) and Choi and Kumar (2024a).

Consider a physical state of a granular flow at time  $t$ ,  $X_t = \{\mathbf{x}_i^t\}_{i \in N}$ , where each  $\mathbf{x}_i^t = [\mathbf{p}_i^{t-k:t}, \mathbf{b}_i^t, \mathbf{f}, \mathbf{w}]$  is the feature of the material point  $i$  in  $N$  total material points. Here,  $\mathbf{p}_i^{t-k:t}$  denotes the material point positions from time  $t - k$  to  $t$ ,  $\mathbf{b}_i^t$  is boundary information,  $\mathbf{f}$  is a categorical identifier for the material point type (e.g., fixed or kinematic), and  $\mathbf{w}$  contains material properties i.e.,  $\mathbf{w} = [\phi_i, c_i]$  for the Mohr-Coulomb materials used in this study.

The GNS represents  $X_t$  as a graph  $G = (V, E)$ , where vertices  $V = \{\mathbf{v}_i\}_{i \in N}$  correspond to material points and edges  $E = \{\mathbf{e}_{i,j}\}_{i \in N, j \in \mathcal{N}(i)}$  describe the interactions between the material point  $i$  and its neighbor  $j$ , where  $\mathcal{N}(i)$  represents the set of vertices connected to the vertex  $i$ . The GNS updates  $G$  to  $G' = (V', E')$  based on the learned local interaction law modeled through a message passing graph neural network (GNN) (Battaglia et al., 2018), and returns the next state  $X_{t+1}$ . The GNS consists of a learned dynamics approximator  $\mathcal{D}_\Theta$  and the update function  $\mathcal{U}$ .  $\mathcal{D}_\Theta$  adopts an encoder-processor-decoder structure. First, the encoder takes  $X_t$  and embeds it into the

latent graph  $G$ . Next, the processor performs message passing with GNN, which propagates the vertices' information to their neighbors along edges, returning the updated graph  $G'$ . This message passing models the momentum or energy exchange between material points. Finally, the decoder extracts the dynamics information  $Y_t = \{\mathbf{y}_i^t\}_{i \in N}$  of the material points from the updated graph  $G'$ . The update function  $\mathcal{U}$  then advances the current state  $X_t$  using the predicted dynamics  $Y_t$  (i.e.,  $X_{t+1} = \mathcal{U}(X_t, Y_t)$ ). GNS recursively predicts the next states until a desired timestep  $k$ , called rollout:

$$X_{t+1} = \text{GNS}(X_t), \quad X_0 \rightarrow X_1 \rightarrow \dots \rightarrow X_k \quad (1)$$

All modules in  $\mathcal{D}_\Theta$ —encoder, processor, and decoder—are implemented as multilayer perceptrons (MLPs) with two hidden layers of 128 units, comprising the learnable parameter set  $\Theta$ . The training objective eq. (2) is to minimize the mean squared error (MSE) between the predicted dynamics  $\mathbf{y}_i^t \in Y_t$  and the ground truth accelerations of material points  $\mathbf{a}_i^t \in A_t$  by optimizing  $\Theta$ .

$$\mathcal{J}(\Theta) = \frac{1}{N} \sum_{i=1}^N \|\mathbf{y}_i^t - \mathbf{a}_i^t\|^2 \quad (2)$$

In this study, we generate the training data using MPM, which will be explained in Section 4.

Once trained, GNS serves as a surrogate for MPM. GNS can simulate a broad range of granular flow configurations not encountered during training, achieving orders-of-magnitude speedup compared to MPM, while retaining physical fidelity by learning the underlying interaction laws that govern granular flow dynamics (Choi and Kumar, 2024a; Zhao et al., 2025).

### 3.2. Inverse analysis framework with differentiable GNS

The inversion is based on a differentiable GNS that uses gradient-based optimization through automatic differentiation (Figure 3). A brief description follows; further details are provided in Choi and Kumar (2024b), Choi et al. (2025), and Baydin et al. (2018).

Given a set of observed granular flow states  $\{X_t^{\text{obs}}\}_{t \in \mathcal{T}}$  at a subset of time indices (e.g.,  $\mathcal{T} \subseteq \{0, 1, \dots, T\}$ ), the goal is to estimate the optimal parameters  $\boldsymbol{\theta}^*$  that minimize the discrepancy between the observed states and the corresponding forward simulation results from GNS:

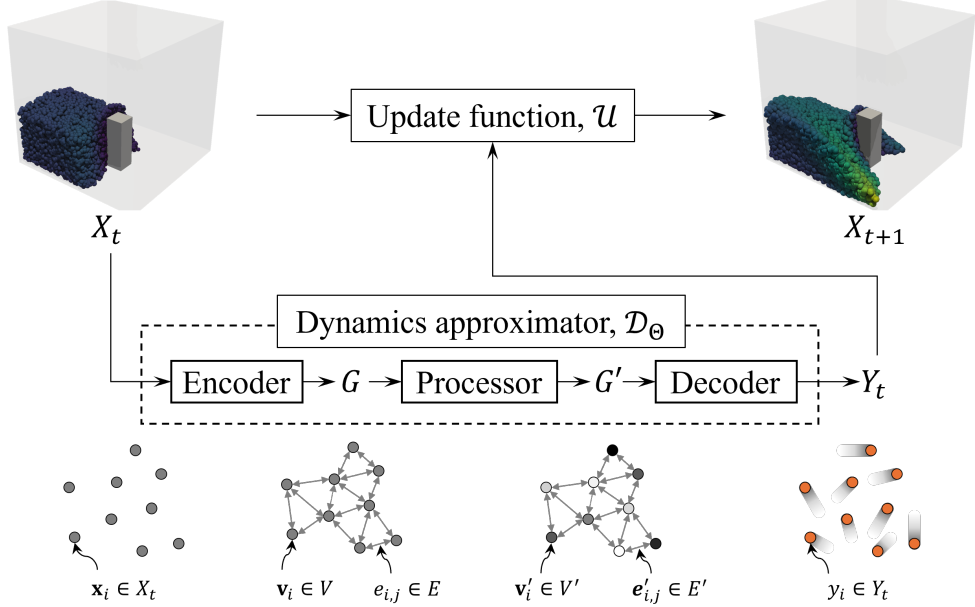


Figure 2: Schematic of the Graph Neural Network Simulator (GNS) architecture.

$$\boldsymbol{\theta}^* = \arg \min_{\boldsymbol{\theta}} \mathcal{L}_{\boldsymbol{\theta}} \left( \{X_t^{\text{obs}}\}_{t \in \mathcal{T}}, \{\hat{X}_t(\boldsymbol{\theta})\}_{t \in \mathcal{T}} \right) \quad (3)$$

Here,  $\hat{X}_t(\boldsymbol{\theta})$  denotes the GNS-simulated granular flow state at time  $t$  under parameters  $\boldsymbol{\theta}$ , and  $\mathcal{L}_{\boldsymbol{\theta}}(\cdot, \cdot)$  is a task-specific loss function measuring the mismatch between observed and simulated states. In this study,  $\boldsymbol{\theta}$  is a set of strength parameters, such as  $S_r$  or friction angle  $\phi$ ;  $\mathcal{L}$  is the runout distance. The time index set  $\mathcal{T}$  refers to the condition with information; in the considered case histories, only the final post-failure geometry is available, in which case  $\mathcal{T} = \{T\}$ .

Diff-GNS solves Equation (3) using gradient-based optimization (Equation (4)). It iteratively improves  $\boldsymbol{\theta}$  using the gradient of the loss  $\mathcal{L}_{\boldsymbol{\theta}}$  with respect to  $\boldsymbol{\theta}$ ,  $\nabla_{\boldsymbol{\theta}} \mathcal{L}_{\boldsymbol{\theta}}$  (Equation (5)).

$$\boldsymbol{\theta}^{(n+1)} \leftarrow \boldsymbol{\theta}^{(n)} - \eta^{(n)} \cdot \mathbf{d}^{(n)} \quad (4)$$

$$\nabla_{\boldsymbol{\theta}} \mathcal{L}_{\boldsymbol{\theta}} = \frac{\partial \mathcal{L}_{\boldsymbol{\theta}} \left( \{X_t^{\text{obs}}\}, \{\hat{X}_t(\boldsymbol{\theta})\} \right)}{\partial \boldsymbol{\theta}} \quad (5)$$

Here,  $n$  is the optimization step,  $\eta^{(n)}$  is the learning rate, and  $\mathbf{d}^{(n)}$  is the update direction, which

is a function of  $\nabla_{\boldsymbol{\theta}} \mathcal{L}_{\boldsymbol{\theta}}$ . Because GNS is implemented as a neural network, it is fully differentiable and allows efficient computation of  $\nabla_{\boldsymbol{\theta}} \mathcal{L}_{\boldsymbol{\theta}}$  using AD.

There is often prior knowledge of feasible parameter ranges. Embedding these bounds in the optimization both reduces the search space and avoids nonphysical solutions. We adopt the L-BFGS-B algorithm (Byrd et al., 1995), a limited-memory quasi-Newton method that supports box constraints of the form  $\boldsymbol{\theta}_{min} \leq \boldsymbol{\theta} \leq \boldsymbol{\theta}_{max}$ , where the bounds reflect prior knowledge. Byrd et al. (1995) provides the L-BFGS-B algorithmic details for interested readers.

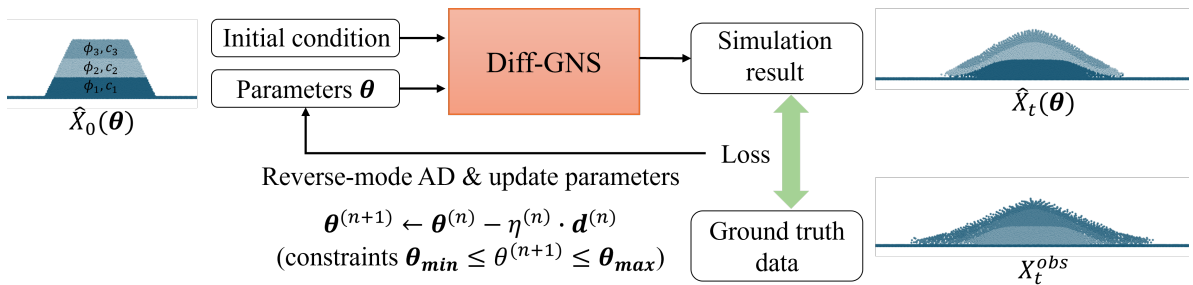


Figure 3: Differentiable graph neural network simulator (Diff-GNS)-based framework for solving inverse problems in granular flows (after Choi et al. (2025)). Given the initial condition and parameters  $\boldsymbol{\theta}$  for a slope system at time 0,  $\hat{\mathbf{X}}_0(\boldsymbol{\theta})$ , Diff-GNS runs the forward simulation and generates  $\hat{\mathbf{X}}_t(\boldsymbol{\theta})$ , granular flow state at time  $t$ . It then evaluates the loss compared to  $\mathbf{X}_t^{obs}$ , the observed state.  $\boldsymbol{\theta}$  is updated using gradient-based optimization with optional given constraints.

### 3.3. Comparison to existing procedures that estimate $Sr$

The Diff-GNS framework has fundamental advantages over existing back-analysis techniques explained in Section 2, addressing their core limitations in physical representation, flexibility, automation, and scalability, as summarized in Table 1.

First, regarding physical fidelity, existing methods rely on simplified assumptions about failure mechanics, such as predefined geometries or slip surfaces. In contrast, the Diff-GNS framework is built upon learned physics of a high-fidelity numerical solver, MPM. This allows Diff-GNS to naturally capture more complex physics-consistent behaviors, while retaining computational efficiency.

Second, Diff-GNS offers greater flexibility in its optimization objective. While all methods (traditional and Diff-GNS) require pre- and post-failure geometries as primary input data, traditional approaches typically target a single, fixed objective, such as matching a final center-of-gravity

displacement or achieving a factor of safety of 1.0. The Diff-GNS loss function, however, can be flexibly defined to incorporate a richer set of observational data, including the displacement, full final runout geometry, intermediate runout stages, or even velocity fields.

Lastly, traditional methods rely on an iterative trial-and-error process that require significant engineering judgment, which limits reproducibility. Diff-GNS replaces this subjective workflow with a fully automated, gradient-based optimization pipeline. This automation not only ensures more reproducibility but also makes the framework inherently scalable to high-dimensional inverse problems without an increase in computational cost with respect to the number of parameters.

#### 4. Data and training

Most previous GNS training datasets were designed for proof-of-concept studies with very simplified geometries (Sanchez-Gonzalez et al., 2020; Choi and Kumar, 2024a; Zhao et al., 2025), such as a cube-shaped homogeneous material in a  $1 \times 1$  m domains. The only effort targeting realistic slopes, Choi et al. (2025), still relied on geometries not informed by case histories and with limitations in geometric scale representation, i.e., small and large slopes cannot be accommodated effectively.

This study addresses these gaps by developing targeted training datasets with geometries informed by runout failure case histories and additional configurations to supplement the training. The datasets expose GNS to various runout mechanisms and adopt a scale-specific strategy (Figure 4) to cover a range of slopes encountered in practice, from a few meters to several hundred meters (Olson, 2001; Weber, 2015). A single GNS cannot efficiently handle this spectrum because its resolution is tied to the material point spacing set by the training data's cell size. Large slopes demand coarser spacing with a larger cell size to stay within GPU memory limits, whereas small slopes require finer spacing for representing adequate detail. We therefore train two complementary GNS models: (i) a large-scale GNS for slopes 200-500 m long and 50-100 m high and (ii) a small-scale GNS for slopes 50-200 m long and 10-50 m high. These ranges are guided by 16 case history failures (Olson, 2001; Weber, 2015), summarized in Table A.2 in Appendix A. The considered cases serve only to guide the training rather than strict limits of applicability; GNS models can

Items	Kinetics method	ZIF	IMM	Diff-GNS
<b>A. Physics and geometrical representation</b>				
Governing physics	$F = ma$ on rigid blocks	Pseudo-static analysis at ZIF condition	$F = ma$ at discrete, user-defined incremental geometries	Learned MPM physics
Runout Development	Pre-defined polynomial curve	Assumed based on ZIF geometry	User-interpreted	Naturally modeled via learned MPM physics
Material interaction	Simplified to rigid blocks	Limited representation at ZIF geometry	Based on assumed geometries	Interaction enabled through learned MPM physics
Deformation modeling	Simplified to block sliding	N/A	Based on assumed geometries	Learned MPM physics
3D potential	Designed for 2D	Designed for 2D	Designed for 2D	Yes
<b>B. Data &amp; input requirements</b>				
Geometry	Pre and post failure geometries	Pre and post failure geometries	Pre, post, and incremental failure geometries	Pre and post failure geometries
Objective	Single: match final center of gravity displacement	Single: limit-equilibrium $FS = 1$ at ZIF condition	Multiple: incremental runout stages	Flexible (e.g., displacement, final/intermediate partial or full geometry)
<b>C. Implementation &amp; Computation</b>				
Optimization pipeline	Trial and error on $S_r$	Manual calibration of ZIF geometry and $S_r$	Manual calibration of incremental geometries and $S_r$	Differentiable simulator with gradient-based optimization
Reproducibility	User dependent	User dependent	User dependent	High: fully automated once GNS is trained
Forward evaluation runtime	Efficient	Efficient, but requires iterative ZIF geometry inference	Significant, requires significant time to define incremental geometries	Efficient
Multi-parameter scalability	Limited	Limited	Limited	Significant

Table 1: Features of traditional methods to estimate  $S_r$  and comparison to Diff-GNS.

generalize to scenarios outside these ranges, as demonstrated in previous studies (Sanchez-Gonzalez et al., 2020; Choi and Kumar, 2024a).

Each model is trained on MPM simulations with cell size and material point resolution tailored to its target scale. Table 2 summarizes the MPM configurations for the large- and small-scale datasets. Both designs ensure at least several thousand material points to represent typical case history slopes (Table A.2) with sufficient detail, while capping the number of material points at 20,000 to avoid GPU memory overflow (Choi and Kumar (2024b)). This dual-scale design mitigates memory bottlenecks, maintains appropriate resolution, and collectively enables proper representation of slope geometries encountered in practice from tens to hundreds of meters—capabilities that prior GNS studies cannot consider.

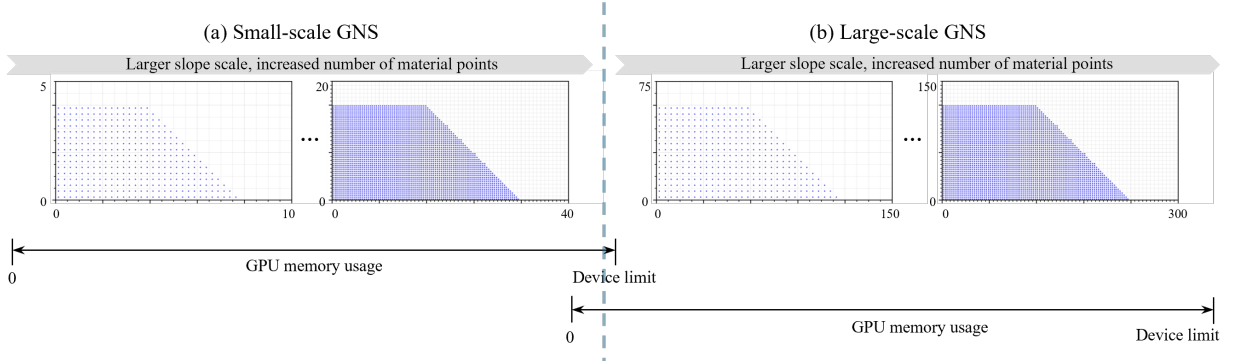


Figure 4: Scale-specific separate GNS training strategy. A single GNS cannot efficiently accommodate the wide range of slope dimensions due to resolution and memory constraints: large slopes require an excessive number of material points, exceeding the GPU device’s memory limits, while small slopes demand finer material point resolution than a large-scale model can provide. We train separate GNS models for large and small-scale slopes, each with its own representative material point and cell resolution of the underlying MPM training data.

Figure 5 presents the five base pre-failure geometries used to generate the training datasets, with material properties summarized in Table 2. The first three geometries (Figure 5a-c) are informed by case histories. Note that rather than replicating the geometries, the intent is to distill geometric traits so the GNS can learn representative runout mechanisms. The training is complemented by the last two scenarios to incorporate a variety of mechanisms in the GNS training. The horizontal and vertical bars at each vertex indicate variations applied to the underlying baseline geometry. The variation ranges are tabulated in Table A.1. These geometric variations introduce diversity into the training dataset.

The first configuration (Figure 5a) is considered to capture generic rounout features in embankments and some dams (e.g., North Dike of Wachusett dam (Olson et al., 2000), Fort Peck dam (Marcuson and Krinitzsky, 1976), Lake Ackerman Highway embankment (Hryciw et al., 1990)). As a reference, Figure 5a shows the geometry of the North Dike of Wachusett dam case history. Regions labeled with the same material index (e.g., soil 1-3) draw their Mohr-Coulomb strength parameters from the same distribution, but do not necessarily share identical properties. These parameters are randomly sampled from uniform distributions in the ranges specified in Table 2. These distributions span the  $S_r$  range and non-liquefied strength documented in Olson (2001). Each geometry contains at least three layers to promote learning of multi-material interactions. Soil 3, representing cohesion-only material, is typically placed in the bottom layers to simulate liquefied zones described by  $S_r$ .

The second configuration (Figure 5b) emulates upstream tailings dam geometries (e.g., Sgurigrad dam (on Large Dams, 2001)) and their corresponding flow failure. Note that the upstream component is simplified for training purposes as schematized in Figure 5b. Liquefaction is triggered at the bottom unit to generate runouts.

The third configuration (Figure 5c) reflects typical zoned dam geometries (Clarkson and Williams, 2021), including distinct core and shell components as observed in case histories (e.g., San Fernando dam (Seed et al., 1973), La Palma dam (Weber, 2015)), and simulates runout scenarios after triggering liquefaction on different components.

The fourth configuration (Figure 5d) includes random slope configurations subject to runout failure, providing additional diversity to the training set. The final configuration (Figure 5e) adds a general spectrum of granular flow dynamics, including collision and frictional shearing generated by the rectangular granular bodies subjected to collide with different imposed initial velocities to further inform runout mechanisms to the trained GNS.

The discussed configurations are randomly generated based on Table A.1. All geometries in Figure 5 are sized for the large-scale GNS; for the small-scale GNS, dimensions are reduced by a factor of four to match the finer material-point spacing required by the smaller MPM cell size.

For effective training, we need to properly select the following GNS-specific hyperparameters:

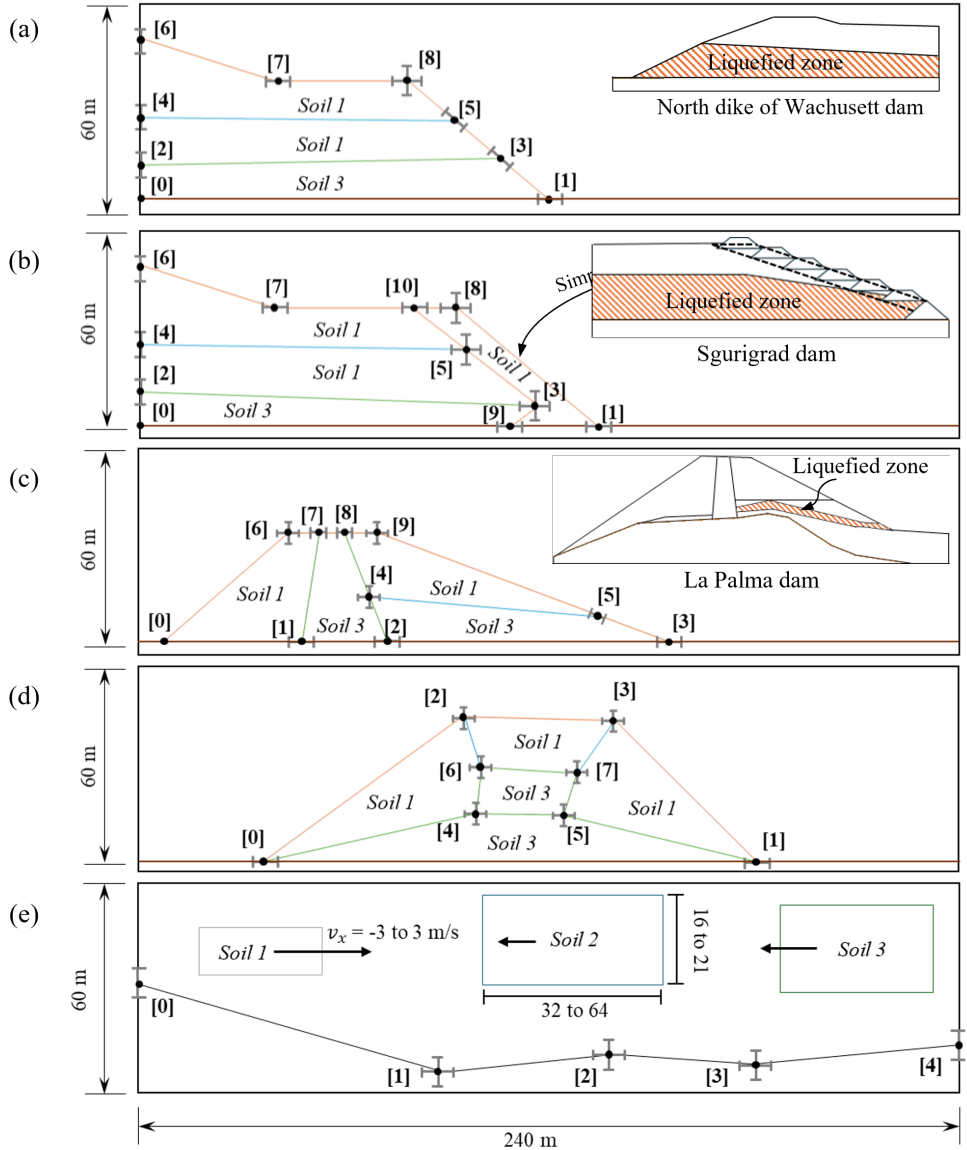


Figure 5: Pre-failure configurations to generate training data for the large-scale GNS. Dimensions for training the small-scale GNS are scaled down by 0.25. The figures are not in scale. (a), (b), and (c) configurations are informed by the case histories listed in Table A.2 in Appendix A. Examples are included as figure insets (i.e., North Dike of Wachusett dam, Sgurigrad dam, La Palma dam). (d) and (e) are additional configurations to complement the GNS learning process (see discussions in the text). The numbers in square brackets indicate the indices of the polygon vertices. Solid lines connecting these vertices define the overall shape of granular masses, with brown solid lines denoting the bedrock boundary. The x and y coordinates of the polygon vertices are randomly perturbed; the bars at each vertex represent the perturbation. Table A.1 in Appendix A provides the variation range for the corresponding vertex indices. Strength properties for Soil 1, Soil 2, and Soil 3 are drawn from distributions in Table 2. In subfigures a-c, the inscribed figures are examples of case histories that we design to emulate. In subfigure e, the black arrow shows the randomly imposed initial velocity.

Table 2: Datasets for training large- and small-scale GNSs.

Property	Dataset	
	Large-scale	Small-scale
MPM configuration	Domain boundary	60 x 240 m
	Cell size	2 x 2 m
	Distance between material points	1 m
	dt	5e-5 s
	# material points per cell	4
	Max. # material points	6,000
Materials	Soil 1	$\phi = 20 - 47^\circ$
	Soil 2	$\phi = 20 - 47^\circ$ , $c = 20 - 50 \text{ kPa}$
	Soil 3	$\phi = 0^\circ$ , $c = 20 - 50 \text{ kPa}$
	Elastic modulus	30 MPa
	Density	1800 ( $\text{kg}/\text{m}^3$ )
	Poisson ratio	0.3
# simulations		2,500

<sup>a</sup> Uniform distributions are used to sample the  $\phi$  and  $S_r$  within the ranges tabulated for soils 1 to 3 and assigned to the corresponding regions in Figure 5.

connectivity radius, number of message passing steps, and noise standard deviation (Sanchez-Gonzalez et al., 2020). The connectivity radius specifies the maximum distance within which two material points are connected by a graph edge for message passing. Larger values capture more local interactions because more neighbors are included in the graph, but increase computational cost. We set the radius to 1.5 times the MPM cell size provided in Table 2. This enables sufficient neighbor connectivity for capturing local interactions in GNS. The number of message passing steps defines how many rounds of message passing occur between connected graph vertices. Increasing this value improves the model’s capacity to capture complex interactions but also raises computational cost. We use 10 steps, which balance the learning capacity and computation cost (Choi and Kumar, 2024a; Sanchez-Gonzalez et al., 2020).

In long rollouts, prediction errors accumulate as the model reuses its own outputs as inputs (Equation (1)), leading the granular flow state away from the training distribution. To mitigate this error accumulation, we employ the random-walk noise injection strategy of Sanchez-Gonzalez et al. (2020). During training, Gaussian noise with a specified standard deviation is added cumulatively

to material point positions in  $\mathbf{x}_i^t$ , while the acceleration targets (Equation (2)) are adjusted so that the perturbed positions still lead to the correct next state. This improves model stability to error accumulation during rollout. We use a velocity noise standard deviation of 0.067 m/s and 0.020 for large and small GNS training, selected based on the overall velocity standard deviation in the respective training dataset. This noise is then applied cumulatively to perturb material point positions. For further implementation details, refer to Sanchez-Gonzalez et al. (2020) and Pfaff et al. (2020). For the other typical deep learning hyperparameters, we use the learning rate of 1e-4 for the Adaptive Moment Estimation (ADAM) optimizer (Kingma, 2014), batch size of 2 with 3 GPUs for the parallel training, yielding the effective batch size of 6. The GPU device is NVIDIA A100, provided by Lonestar 6 at the Texas Advanced Computing Center (TACC).

Figure 6 shows the training loss (Equation (2)) history for the large and small-scale GNS. In both cases, the mean squared error (MSE) decreases rapidly during the initial training phase, followed by a gradual reduction and stabilization as training progresses. The large-scale GNS converges to a higher final loss compared to the small-scale GNS, since it typically has a higher acceleration level due to the larger system scale. The training time for 3.5 million steps takes about 4 days, corresponding to the end of the GPU runtime on the computing cluster used in this study.

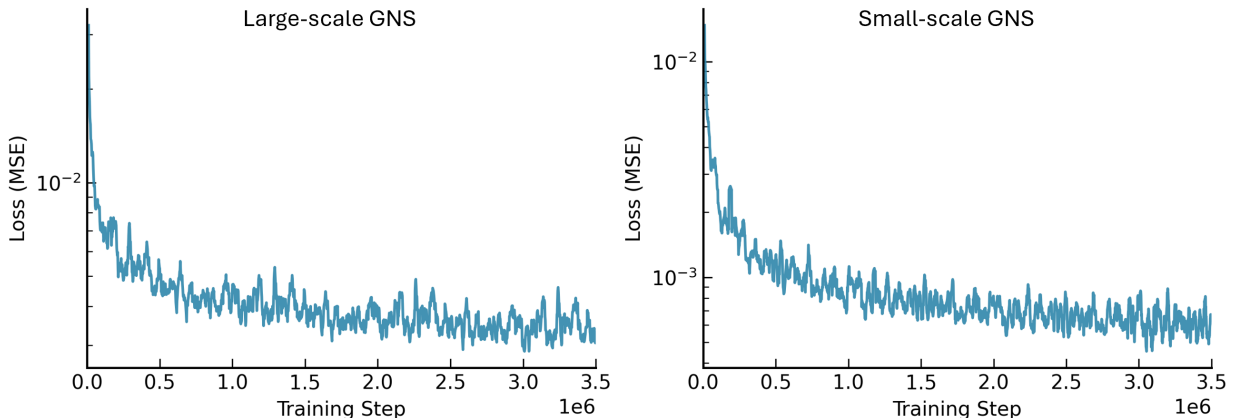


Figure 6: Training loss history.

## 5. Diff-GNS framework performance in case histories

We evaluate the performance of the Diff-GNS framework for large and small-scale slopes by back-analyzing  $S_r$  for two liquefaction-induced flow failure case histories: the Lower San Fernando dam and La Marquesa dam. Brief overviews of these cases are provided in Appendix B. The discussions in this section focus on the GNS modeling setup and performance assessment. Importantly, none of the case histories, their specific stratigraphy, or material configurations were included in the training dataset; hence, they offer a basis for assessing the Diff-GNS framework on unseen scenarios.

### 5.1. Lower San Fernando dam

Figure 7 shows the pre- and post-failure configurations from Weber (2015) for the Lower San Fernando dam used for the GNS simulations. The model contains 6,256 material points. Given the dam's large size (over 200 m in length), we employ the large-scale GNS model. For simplicity, the drain layer is merged with the berm material (see Figure A.2). Previous studies (Olson, 2001; Weber, 2015) report uncertainties in the friction angles of ground shale (material 6) and rolled fill (material 7). Hence, the inversion in the Diff-GNS simultaneously estimates the residual strength  $S_r$  of material 1 (liquefied upstream hydraulic fill) and the friction angles of materials 6 and 7. The goal is to identify the parameter set that can explain the observed runout. Field observations indicate runouts between 42 m and 65 m (Talbot et al., 2024); we adopt 53 m as the target. Initial guesses are  $S_r = 30$  kPa for material 1 and friction angles of  $30^\circ$  for materials 6 and 7, with bounds of  $27^\circ$ - $33^\circ$  and  $27^\circ$ - $37^\circ$ , respectively.  $S_r$  is treated as an operative strength representing the average resistance during the failure process. Unlike earlier back-analyses that only inferred  $S_r$ , the Diff-GNS can jointly estimate three interacting parameters. Other material properties are summarized in Table 3.

The optimization history (Figure 8) shows the data loss, defined as the squared error between simulated and observed runout, falling below a pre-defined tolerance of  $10^{-1}$ , m<sup>2</sup> by the fourth iteration. The inferred  $S_r$  for material 1 converges to 18.9 kPa, in close agreement with the 18.7 kPa estimate of Olson (2001), while the friction angles for materials 6 and 7 converge to  $28.9^\circ$

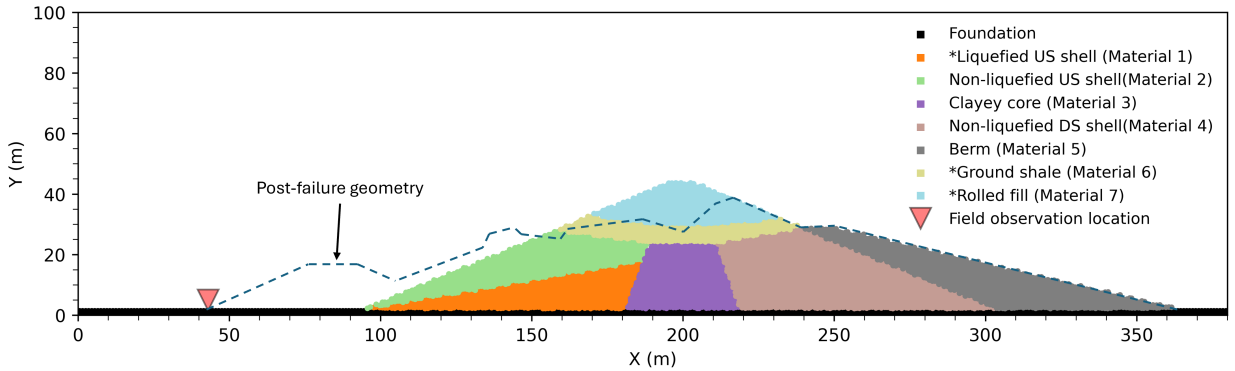
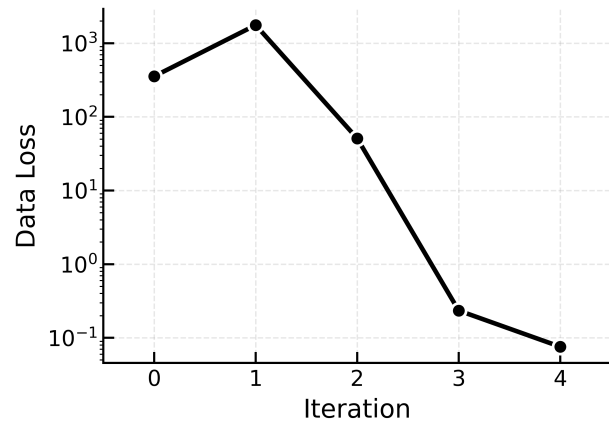


Figure 7: Pre- and post-failure configuration of the Lower San Fernando dam for GNS forward simulation. The asterisk (\*) in the legend denotes the materials for which strengths are back-calculated.

and  $32.8^\circ$ , respectively (Figure 8b), which are within the uncertainty ranges of  $27^\circ$ - $33^\circ$  and  $27^\circ$ - $37^\circ$  for materials 6 and 7 in (Olson, 2001; Weber, 2015). The evolving geometries (Figure 9) show the simulated runout progressively matching the target runout distance. Figure 9 illustrates that iteration 0 underestimates the target distance, iteration 1 overestimates it, and by iteration 4,  $S_r$  converges to a value that minimizes the data loss. At this stage, the predicted runout geometry is consistent with the target runout and represents the post-failure geometry reasonably well.

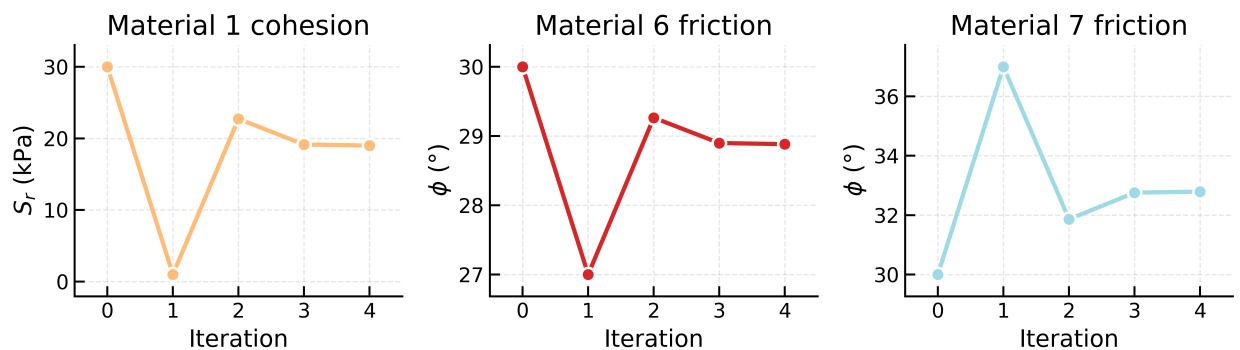
The GNS simulation reproduces key deformation features highlighted in Figure A.2. For instance, the upstream shell undergoes major displacement and extrusion, while the downstream shell and berm remain largely intact, and the clay core forms a tongue-like protrusion on the left flank. The crest settles 20 m, consistent with the value reported by Olson (2001) and Talbot et al. (2024). These patterns mirror prior MPM-based modeling for the Lower San Fernando dam (Feng et al., 2021; Talbot et al., 2024; Tjung and Soga, 2021).

Finally, to further validate the Diff-GNS results, we ran a high-fidelity MPM simulation using the Diff-GNS-inferred  $S_r$  and friction angles. The resulting geometry evolution (Figure 10) closely matches the GNS prediction, including the extent of runout (within  $\sim 1$  m error) and the characteristic deformation features, confirming that the back-calculated parameters are physically sound.



(a) Data loss

space1em



(b) Material parameter history

Figure 8: Diff-GNS optimization history for the Lower San Fernando dam.

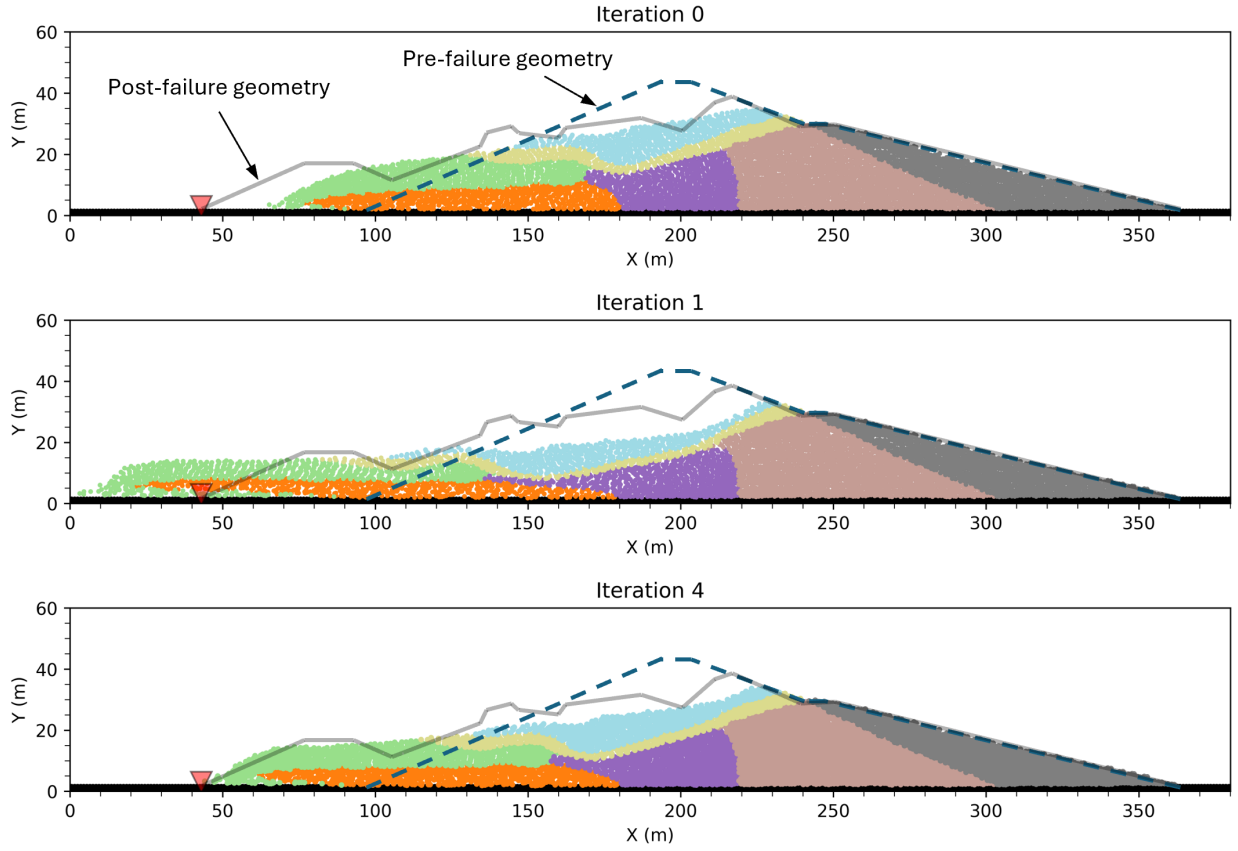


Figure 9: Post-failure geometry evolution throughout the optimization of material parameters for the Lower San Fernando dam. The red inverted triangle indicates the field observed runout. The dashed line represents the pre-failure geometry.

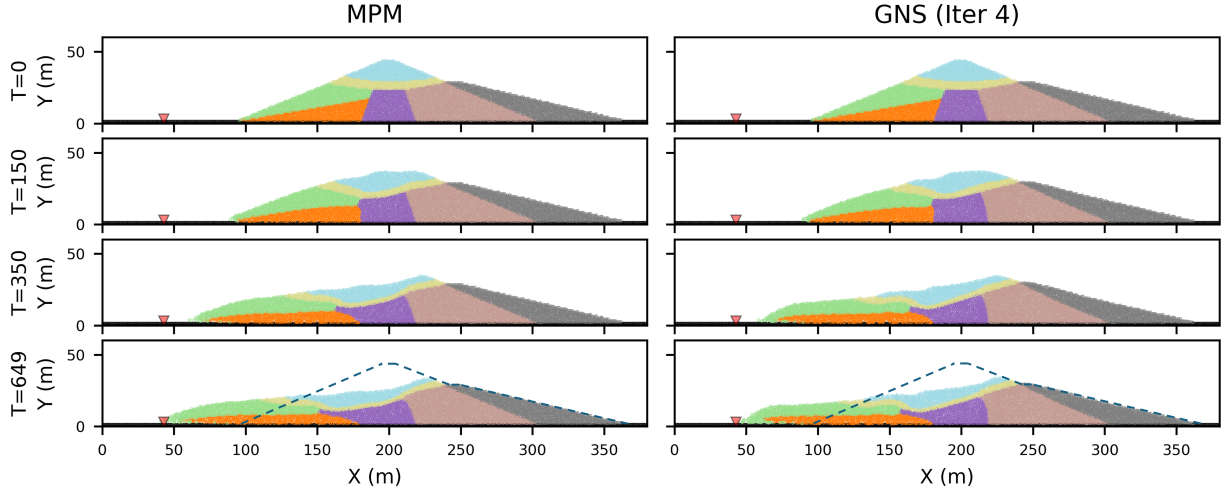


Figure 10: MPM simulation of the Lower San Fernando dam with inferred material properties compared to GNS at optimization iteration 4.

ID	Description	$\phi$ (°)	$c$ (kPa)
Material 1	Liquefied US shell (back-calculating)	0	30 (Initial guess)
Material 2	Non-liquefied US shell	35	1
Material 3	Clayey core	0	30
Material 4	Non-liquefied DS shell	35	1
Material 5	Berm	37	0
Material 6	Ground shale (back-calculating with constraint range 27–33°)	30 (Initial guess)	1
Material 7	Rolled fill (back-calculating with constraint range 27–33°)	30 (Initial guess)	1

Table 3: Material properties used in analysis for the Lower San Fernando dam.

### 5.2. La Marquesa dam

Figure 11 shows the pre- and post-failure configuration used for the Diff-GNS simulations for the La Marquesa dam, modeled with 8,794 material points. Because the dam is relatively small (length  $< 50$  m), the small-scale GNS model is used. Previous studies (Olson, 2001; Weber, 2015) treated the liquefied silty sands (materials 1 and 2) and the saturated silty/clayey sand shell (material 6) as a single zone with one residual strength  $S_r$ . This simplification reflects the difficulty of manually calibrating multiple parameters. In our analyses, Diff-GNS performs a more challenging inversion by independently inferring  $S_r$  for materials 1, 2, and 6, which are initialized with  $S_r$  of 11 kPa. Table 4 lists the material properties. The runouts from available post-failure geometries Olson (2001) are estimated as 2.5 m for the upstream slope and 10 m for the downstream slope as indicated by the inverted red triangles in Figure 11.

Figure 12 shows the optimization history. The data loss generally decreases and stabilizes by iteration 13, with a temporary increase between iterations 7 and 8. The optimized  $S_r$  values converge to 4.2 kPa (material 1), 4.6 kPa (material 2), and 4.00 kPa (material 6), all within the 2.2–9.8 kPa range reported by Olson (2001), and only slightly below their best estimate of 5 kPa. Figure 13 illustrates the runout evolution. At iteration 0, runouts deviate from the targets, and no significant deformations are observed. As optimization proceeds, both upstream and downstream runouts approach the observed targets (red inverted triangles). By iteration 13, the simulated runouts match the observations reasonably well.

The final GNS simulation reproduces the key features of the case history (Figure A.3), including the extrusion of liquefied materials on both sides and mobilization of the overlying shell. However, it does not replicate the  $\sim 2$  m settlement of the clay core, likely because its undrained shear

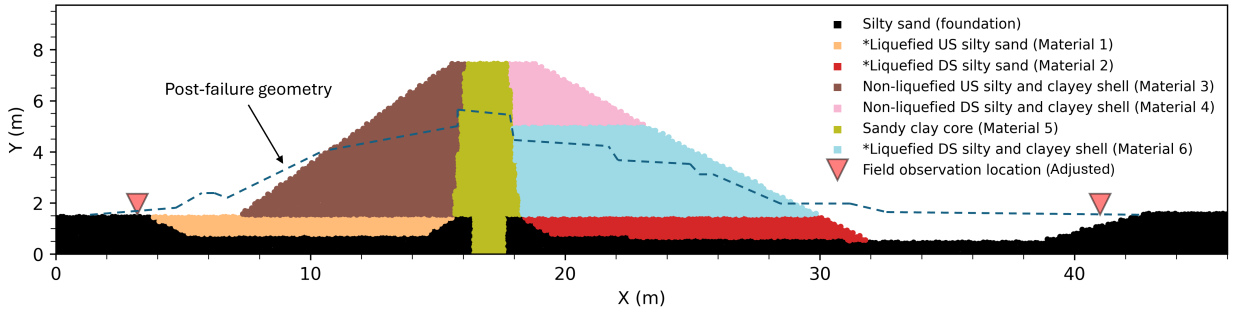


Figure 11: Pre- and post-failure configuration of the La Marquesa dam for GNS forward simulation. The asterisk (\*) in the legend denotes the materials for which strengths are back-calculated.

strength was assigned as a single value. In field conditions, it is likely that the less confined upper core may have mobilized lower strength and settled more than captured here.

We ran an MPM simulation using the inferred  $S_r$  values to further assess the Diff-GNS performance. Figure 14 shows that the MPM results closely follow the Diff-GNS estimations, reproducing the key runout characteristics. Similar to the Diff-GNS, MPM does not capture the vertical core settlement, but it shows a slight leftward core inclination and greater downstream deformation, including more pronounced extrusion of material 1. Despite these minor differences, Diff-GNS efficiently provides physically consistent strength parameters and post-failure runout developments compared to the MPM high-fidelity modeling.

ID	Description	$\phi$ (°)	$c$ (kPa)
Material 1	Liquefied US silty sand (back-calculating)	0	11 (Initial guess)
Material 2	Liquefied DS silty sand (back-calculating)	0	12 (Initial guess)
Material 3	Non-liquefied DS silty and clayey shell	30	0.1
Material 4	Non-liquefied US silty and clayey shell	30	0.1
Material 5	Sandy clay core (back-calculating)	0	24
Material 6	Liquefied US silty and clayey shell	0	10.5 (Initial guess)

Table 4: Material properties used in analysis for the La Marquesa dam.

### 5.3. Computational efficiency

Table 5 shows the computation times for an optimization iteration using Diff-GNS. We also tabulated the MPM forward simulation time for comparison. GNS computation is on RTX 2000

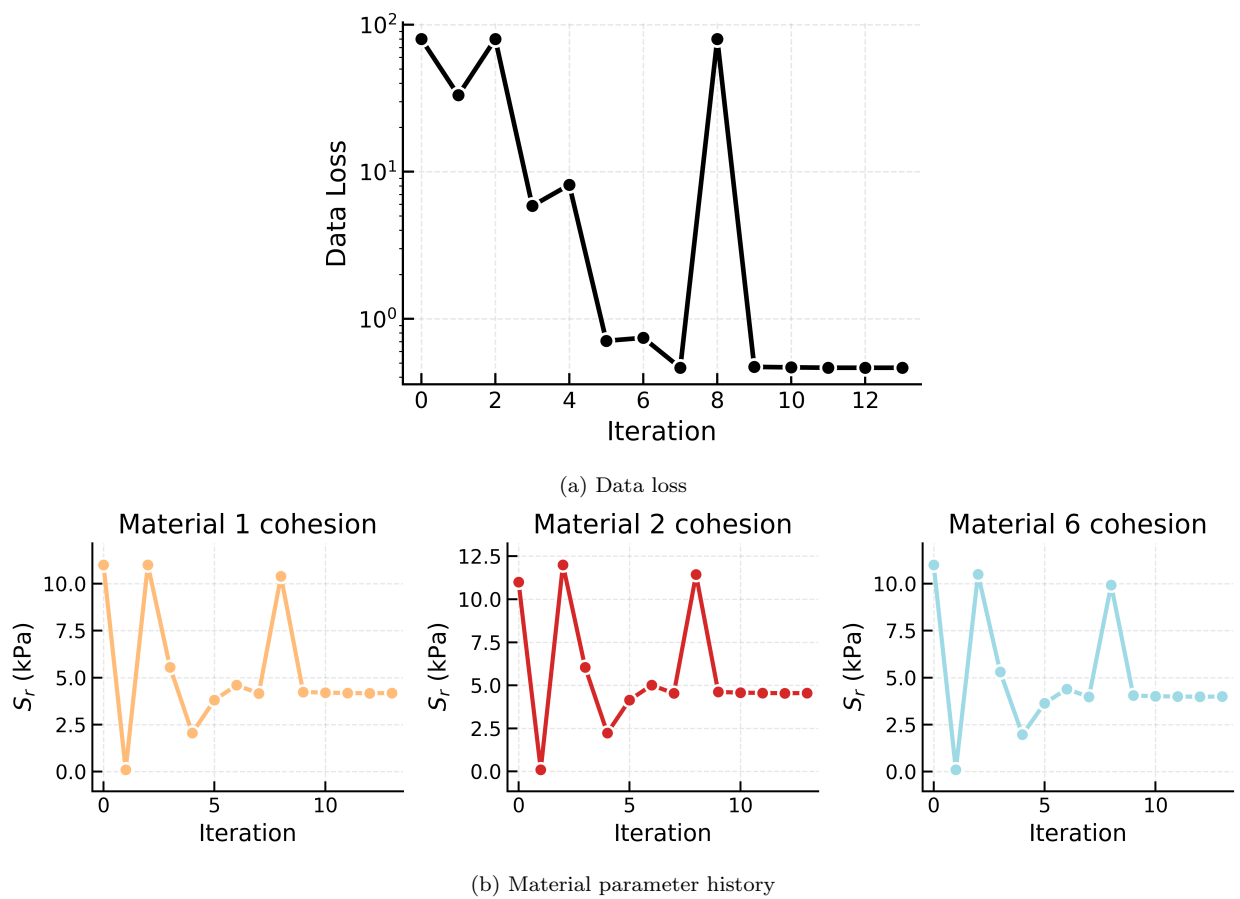


Figure 12: Diff-GNS optimization history for the La Marquesa dam.

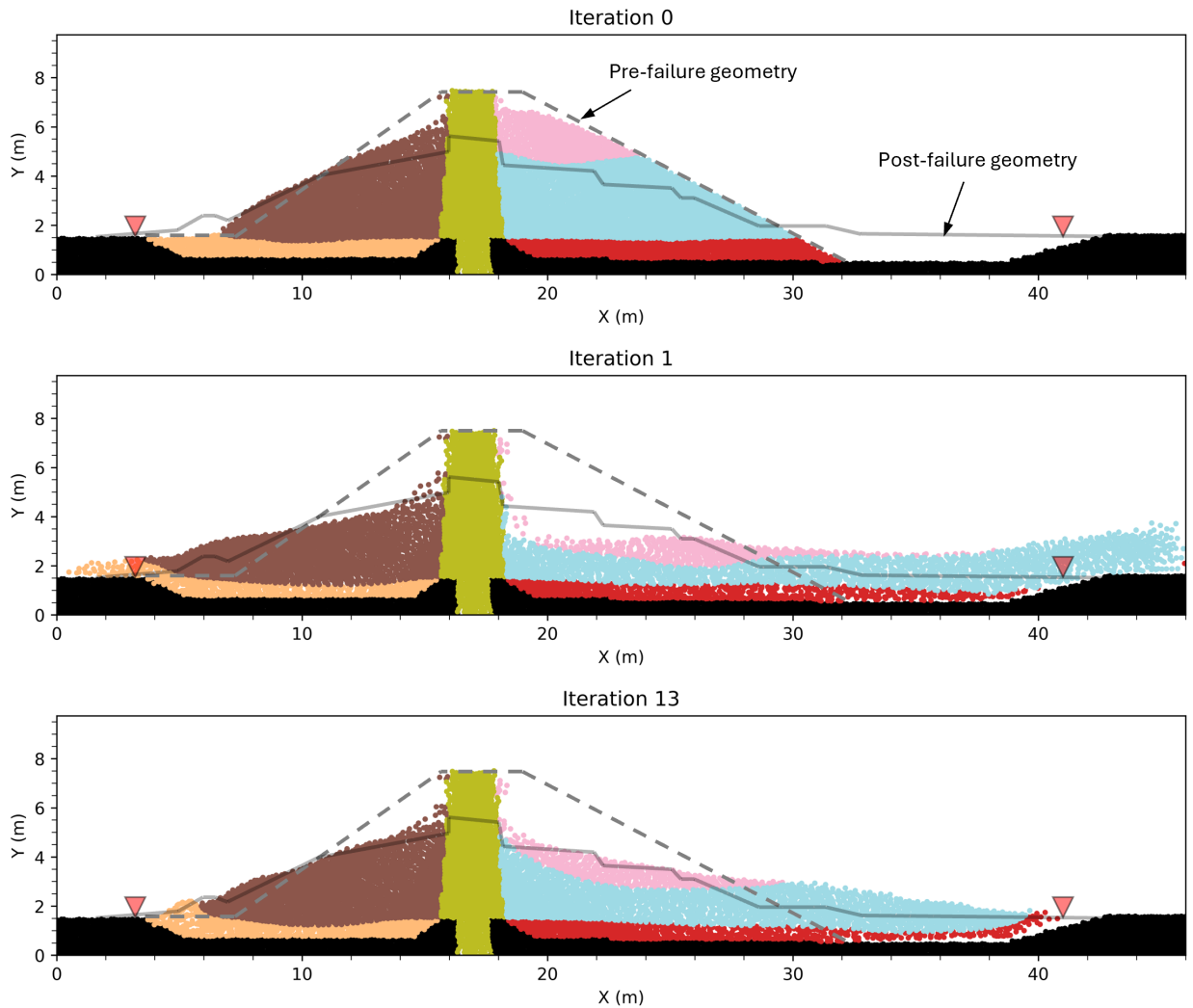


Figure 13: Post-failure geometry evolution throughout the optimization of material parameters for the La Marquesa dam. The red inverted triangle indicates the field observed runout. The dashed line represents the pre-failure geometry.

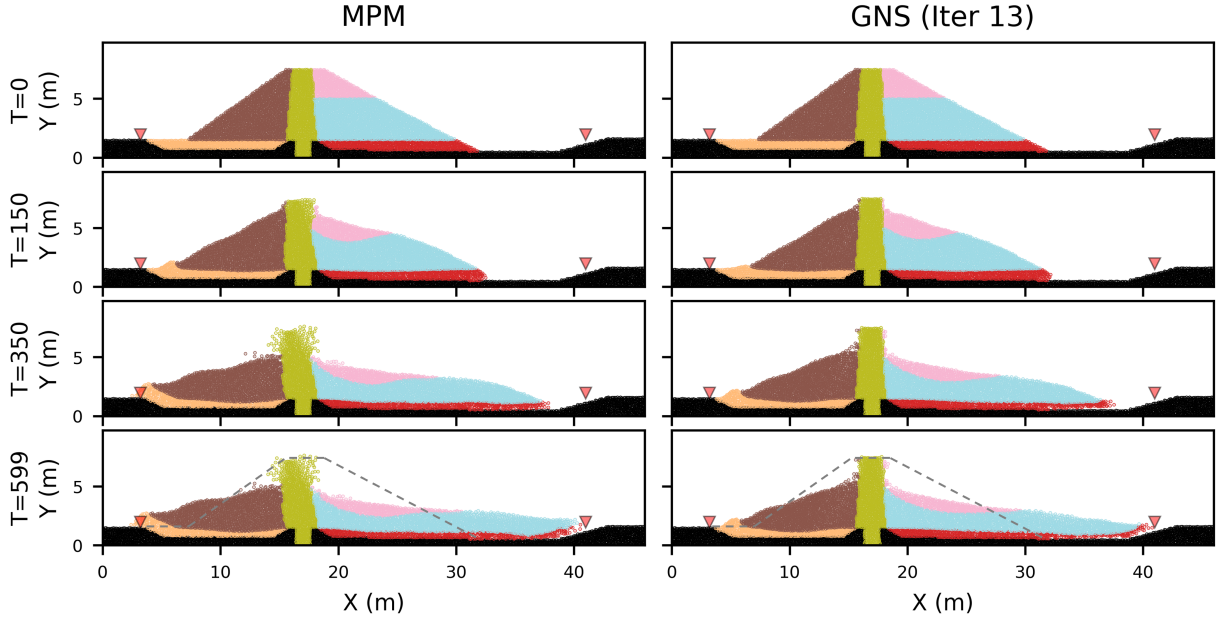


Figure 14: MPM simulation of the La Marquesa dam with inferred material properties compared to GNS at optimization iteration 4.

with 16 GB memory, and MPM computation is on Intel Xeon with 56 cores in the TACC Frontera system. The optimization iteration consists of forward simulation and backpropagation to compute the gradient.

In the case of the Lower San Fernando dam, the MPM forward computation time takes about 1 h, whereas the GNS forward simulation takes about 1 minute, achieving about  $\times 67$  speed up. The backpropagation takes about 3 times the forward simulation, i.e., 180 s, so a full optimization loop finishes in about 4 min. For the La Marquesa dam, computation times scale proportionally with the number of material points. The MPM forward simulation takes about 1.2 h, while the GNS forward run requires about 1 min plus 3.4 min for backpropagation, for a total of roughly 4.4 min optimization time.

Diff-GNS computes the multi-dimensional gradient through a single forward simulation with AD. Consequently, the gradient computation time remains constant regardless of the number of parameters, making the framework scalable to high-dimensional inverse problems, i.e., it can be accommodated for inverting a large number of parameters, if needed. In contrast, in MPM, each parameter would require several forward runs, increasing computational costs significantly.

Table 5: Computation time in the Diff-GNS inversion for the considered case histories compared to MPM forward simulation time.

Case	# Material Points	MPM Sim. (s)	# GNS Steps	GNS Sim. (s)	Gradient (s)	Total (s)
Lower San Fernando dam	6,254	3,867	700	57	180	237
La Marquesa dam	8,794	4,331	650	68	204	272

## 6. Conclusions

This study introduces Diff-GNS as a physics-informed and automated framework for back-calculating post-liquefaction residual strength ( $S_r$ ). The framework addresses key limitations of traditional approaches, which often rely on simplified physics and labor-intensive, subjective workflows. Diff-GNS requires comparable or fewer inputs than traditional approaches Table 1 while providing a physically consistent and computationally efficient alternative. It also supports the simultaneous inversion of multiple parameters—capabilities that are difficult to achieve with traditional approaches.

The framework leverages a trained GNS combined with gradient-based optimization through automatic differentiation for the efficient  $S_r$  inversion. Addressing limitations from previous GNS-focused efforts, this study trains GNSs for small-scale and large-scale slope systems; the training is informed by case history slope failures and complemented by scenarios that bring a variety of runout mechanisms.

The framework performance for small and large-scale slopes is assessed considering two case histories: the Lower San Fernando and La Marquesa dams. The results show a good performance. Diff-GNS estimated  $S_r$  and additional uncertain strength parameters in close agreement with published values. Moreover, it provided a physics-informed runout evolution with a final runout consistent with field observations. Diff-GNS is also significantly more efficient compared to high-fidelity numerical tools such as MPM, which would require several manual iterations to estimate  $S_r$ . For instance, the GNS forward simulations in this study are approximately 100 times faster than MPM. Based on the evaluated case histories, a complete Diff-GNS inversion iteration (forward simulation and back-propagation) is expected to take between 2 to 4 minutes with a single GPU. The discussed framework and the trained GNSs are also amenable to future refinements. For example, fine-tuning could be conducted in the future with additional training data if required.

Overall, the work conducted in this study moves Diff-GNS from conceptual validations toward a practical tool for estimating  $Sr$  and simulating runout in slope systems. The discussed framework lays the groundwork for a new paradigm in back-analysis of case histories of slope failures. Future studies further examining the performance of the discussed framework and the trained GNSs for a large number of case histories are encouraged.

## 7. Acknowledgment

This material is based upon work supported by the National Science Foundation (NSF) under Grant No. 2145092. Any opinions, findings, conclusions, or recommendations expressed in this material are those of the author(s) and do not necessarily reflect the views of the National Science Foundation. The authors acknowledge the Texas Advanced Computing Center (TACC) at The University of Texas at Austin for providing Frontera and Lonestar6 HPC resources to support GNS training (<https://www.tacc.utexas.edu>).

## 8. Competing interests

The authors declare there are no competing interests.

## 9. Availability of data

Data generated or analyzed during this study are available from the corresponding author upon reasonable request.

## References

Abram, G., Solis, A., Liang, Y., Kumar, K., 2022. In situ visualization of regional-scale natural hazards with galaxy and material point method. *Computing in Science & Engineering* 24, 31–39.

Battaglia, P.W., Hamrick, J.B., Bapst, V., Sanchez-Gonzalez, A., Zambaldi, V., Malinowski, M., Tacchetti, A., Raposo, D., Santoro, A., Faulkner, R., 2018. Relational inductive biases, deep learning, and graph networks. *arXiv preprint arXiv:1806.01261* .

Baydin, A.G., Pearlmutter, B.A., Radul, A.A., Siskind, J.M., 2018. Automatic differentiation in machine learning: a survey. *Journal of Machine Learning Research* 18, 1–43.

Byrd, R.H., Lu, P., Nocedal, J., Zhu, C., 1995. A limited memory algorithm for bound constrained optimization. *SIAM Journal on scientific computing* 16, 1190–1208.

Castro, G., Seed, R.B., Keller, T.O., Seed, H.B., 1992. Steady-state strength analysis of lower san fernando dam slide. *Journal of Geotechnical Engineering* 118, 406–427.

Ceccato, F., Yerro, A., Di Carluccio, G., 2024. Simulating landslides with the material point method: Best practices, potentialities, and challenges. *Engineering Geology* , 107614.

Choi, Y., Kumar, K., 2023. Three-dimensional granular flow simulation using graph neural network-based learned simulator, in: *Geo-Congress 2024*, pp. 335–344.

Choi, Y., Kumar, K., 2024a. Graph neural network-based surrogate model for granular flows. *Computers and Geotechnics* 166, 106015.

Choi, Y., Kumar, K., 2024b. Inverse analysis of granular flows using differentiable graph neural network simulator. *Computers and Geotechnics* 171, 106374.

Choi, Y., Macedo, J., Liu, C., 2025. Differentiable graph neural network simulator for forward and inverse modeling of multi-layered slope system with multiple material properties. *arXiv preprint arXiv:2504.15938* .

Chowdhury, K.H., 2018. Evaluation of the state of practice regarding nonlinear seismic deformation analyses of embankment dams subject to soil liquefaction based on case histories. University of California, Berkeley.

Clarkson, L., Williams, D., 2021. An overview of conventional tailings dam geotechnical failure mechanisms. *Mining, Metallurgy & Exploration* 38, 1305–1328.

De Alba, P.A., Seed, H.B., Retamal, E., Seed, R.B., 1988. Analyses of dam failures in 1985 chilean earthquake. *Journal of Geotechnical Engineering* 114, 1414–1434.

De Vaucorbeil, A., Nguyen, V.P., Sinaie, S., Wu, J.Y., 2020. Material point method after 25 years: Theory, implementation, and applications. *Advances in applied mechanics* 53, 185–398.

Feng, K., Wang, G., Huang, D., Jin, F., 2021. Material point method for large-deformation modeling of coseismic landslide and liquefaction-induced dam failure. *Soil Dynamics and Earthquake Engineering* 150, 106907.

Hryciw, R.D., Vitton, S., Thomann, T.G., 1990. Liquefaction and flow failure during seismic exploration. *Journal of Geotechnical Engineering* 116, 1881–1899.

Kingma, D.P., 2014. Adam: A method for stochastic optimization. *arXiv preprint arXiv:1412.6980* .

Kramer, S.L., Wang, C.H., 2015. Empirical model for estimation of the residual strength of liquefied soil. *Journal of Geotechnical and Geoenvironmental Engineering* 141, 04015038.

on Large Dams, I.C., 2001. Tailings dams: risk of dangerous occurrences: lessons learnt from practical experiences. 121, United Nations Publications.

Macedo, J., Yerro, A., Cornejo, R., Pierce, I., 2024a. Cadia tsf failure assessment considering triggering and post-triggering mechanisms. *Journal of Geotechnical and Geoenvironmental Engineering* 150, 04024011.

Macedo, J., Yerro, A., Cornejo, R., Pierce, I., 2024b. Cadia tsf failure assessment considering triggering and post-triggering mechanisms. *Journal of Geotechnical and Geoenvironmental Engineering* 150, 04024011.

Marcuson, W.F., Krinitzsky, E., 1976. Dynamic analysis of Fort Peck dam. US Department of Defense, Department of the Army, Corps of Engineers ....

Moss, R., Gebhart, T., Frost, D., Ledezma, C., 2019. Flow-failure case history of the las palmas, chile, tailings dam. Pacific Earthquake Engineering Research Center PEER report 1.

Olson, S.M., 2001. Liquefaction analysis of level and sloping ground using field case histories and penetration resistance. University of Illinois at Urbana-Champaign.

Olson, S.M., Stark, T.D., 2002. Liquefied strength ratio from liquefaction flow failure case histories. Canadian Geotechnical Journal 39, 629–647.

Olson, S.M., Stark, T.D., Walton, W.H., Castro, G., 2000. 1907 static liquefaction flow failure of the north dike of wachusett dam. Journal of Geotechnical and Geoenvironmental Engineering 126, 1184–1193. doi:10.1061/(ASCE)1090-0241(2000)126:12(1184).

Pfaff, T., Fortunato, M., Sanchez-Gonzalez, A., Battaglia, P., 2020. Learning mesh-based simulation with graph networks, in: International conference on learning representations.

Poulos, S.J., Castro, G., France, J.W., 1985. Liquefaction evaluation procedure. Journal of Geotechnical Engineering 111, 772–792.

Sanchez-Gonzalez, A., Godwin, J., Pfaff, T., Ying, R., Leskovec, J., Battaglia, P., 2020. Learning to simulate complex physics with graph networks, in: International conference on machine learning, PMLR. pp. 8459–8468.

Seed, H., Lee, K., Idriss, I., Makdisi, F., 1973. Analysis of the slides in the san fernando dams during the earthquake of february 9, 1971, report no. eerc 73-2. Earthquake Engineering Research Center, Univ. of California, Berkeley, Calif .

Seed, H.B., 1987. Design problems in soil liquefaction. Journal of Geotechnical Engineering 113, 827–845.

Seed, H.B., Idriss, I.M., Lee, K.L., Makdisi, F.I., 1975. Dynamic analysis of the slide in the lower san fernando dam during the earthquake of february 9, 1971. Journal of the Geotechnical Engineering division 101, 889–911.

Seed, H.B., Seed, R.B., Harder, L.F., Jong, H.L., 1989. Re-Evaluation of the Lower San Fernando Dam; Report 2: Examination of the Post-Earthquake Slide of February 9, 1971. Technical Report. Waterways Experiment Station (U.S.).

Seed, R., Harder Jr, L., 1990. Spt-based analysis of cyclic pore pressure generation and undrained residual strength": Proc., hb seed memorial symp., vol. 2.

Talbot, L.E., Given, J., Tjung, E.Y., Liang, Y., Chowdhury, K., Seed, R., Soga, K., 2024. Modeling large-deformation features of the lower san fernando dam failure with the material point method. Computers and Geotechnics 165, 105881.

Tjung, E., Soga, K., 2021. Liquefaction-induced dam failure simulation—a case for the material point method. arXiv preprint arXiv:2111.13584 .

Weber, J.P., 2015. Engineering evaluation of post-liquefaction strength. University of California, Berkeley.

Zhao, S., Chen, H., Zhao, J., 2025. A physical-information-flow-constrained temporal graph neural network-based

simulator for granular materials. Computer Methods in Applied Mechanics and Engineering 433, 117536.

## Appendix A. Training data

Table A.1: Coordinates of the polygon points in Figure 5.

Point ID	X (m)	Y (m)
<b>Figure 5a</b>		
[0]	0	2
[1]	120 to 130	2
[2]	0	17
[3]	1/3 interpolation between [1] and [8]	1/3 interpolation between [1] and [8]
[4]	0	34
[5]	2/3 interpolation between [1] and [8]	2/3 interpolation between [1] and [8]
[6]	0	Y of [8] + (-2.5 to 10)
[7]	70 to 80	Y of [8]
[8]	70 to 80	37 to 47
<b>Figure 5b</b>		
[0]	0	2
[1]	X of [1] – (20 to 30)	2
[2]	0	17
[3]	1/3 interpolation between [1] and [8] – (5 to 10)	1/3 interpolation between [1] and [8]
[4]	0	32
[5]	2/3 interpolation between [1] and [8] – (5 to 10)	2/3 interpolation between [1] and [8]
[6]	0	Y of [8] + (-5 to 20)
[7]	35 to 40	Y of [8]
[8]	70 to 80	37 to 47
[9]	X of [1] – (10 to 15)	2
[10]	X of [8] – (5 to 10)	Y of [8]
<b>Figure 5c</b>		
[0]	5	2
[1]	0.2 to 0.3 interpolation between [0] and [3]	2
[2]	0.5 to 0.6 interpolation between [0] and [3]	2
[3]	135 to 180	2
[4]	0.4 to 0.6 interpolation between [8] and [2]	0.4 to 0.6 interpolation between [8] and [2]
[5]	0 to 0.6 interpolation between [3] and [9]	0 to 0.6 interpolation between [3] and [9]
[6]	X of [0] + (40 to 50)	35 to 50
[7]	0.1 to 0.45 interpolation between [6] and [9]	0.1 to 0.45 interpolation between [6] and [9]
[8]	0.5 to 0.9 interpolation between [6] and [9]	0.5 to 0.9 interpolation between [6] and [9]
[9]	75 to 90	Y of [6]
<b>Figure 5d</b>		
[0]	50 to 70	2
[1]	170 to 180	2
[2]	90 to 110	37 to 47
[3]	130 to 150	37 to 47
[4] to [7]	Random inside the polygon	Random inside the polygon
<b>Figure 5e</b>		
[0]	0	2 to 16
[4]	240	2 to 16
[1] to [3]	0 to 240	2 to 16

Table A.2: Slope system dimensions of 16 liquefaction-induced flow failure case histories approximated from Olson (2001), Weber (2015), Macedo et al. (2024b), and Moss et al. (2019).

Case history name	Length (m)	Height (m)	Informing training data
Hachiro-Gata Roadway Embankment	30	3.81	Figure 5a
La Marquesa Dam	26	8	Figure 5c
Lake Ackerman Highway Embankment	42	9	Figure 5a
Chonan Middle School	33	9	Figure 5a
Route 272 Roadway Embankment	22.5	9	Figure 5a
Uetsu Line Railway Embankment	45	9.3	Figure 5a
La Palma Dam	42	12	Figure 5c
Shibecha-Cho Embankment	75	15	Figure 5a
Las Palmas Dam	220	15	Figure 5b
Soviet Tajik Slope	135	29.4	Figure 5a
North Dike of Wachusett Dam	120	30	Figure 5a
Takarazuka Landslide	180	30	Figure 5a
Lower San Fernando Dam	240	53	Figure 5c
Fort Peck Dam	450	60	Figure 5a
Calaveras Dam	385	75	Figure 5c
Cadia Dam	300	80	Figure 5b

## Appendix B. Descriptions of case histories

### *Lower San Fernando dam*

The Lower San Fernando dam experienced a catastrophic liquefaction-induced flow failure during the 1971 San Fernando earthquake in California fig. A.1. Previous studies (Seed et al., 1973, 1975; Olson, 2001) indicated that liquefaction in hydraulic fill material of the upstream slope is the main cause of dam failure. Post-earthquake inspections revealed that a substantial portion of the upstream (US) shell and core were mobilized, leaving only 1-2 meters of freeboard. In response, authorities conducted an emergency drawdown of the reservoir and evacuated approximately 80,000 downstream residents. The displaced mass traveled approximately 42–65 meters into the reservoir (Talbot et al., 2024), similar to the dam’s original height, and the crest experienced vertical settlements of up to 20 meters, underscoring the severity of deformation. This case has since become one of the most well-studied examples of liquefaction-induced flow failure and serves as a canonical benchmark for evaluating  $S_r$  through back-analysis.

Figure A.2 shows the pre- and post-failure geometry of the dam. It consists of rolled fill, ground shale, clay core, upstream hydraulic fill, downstream hydraulic fill, drain blanket, and berm. The



Figure A.1: Lower San Fernando dam failure (Chowdhury, 2018)

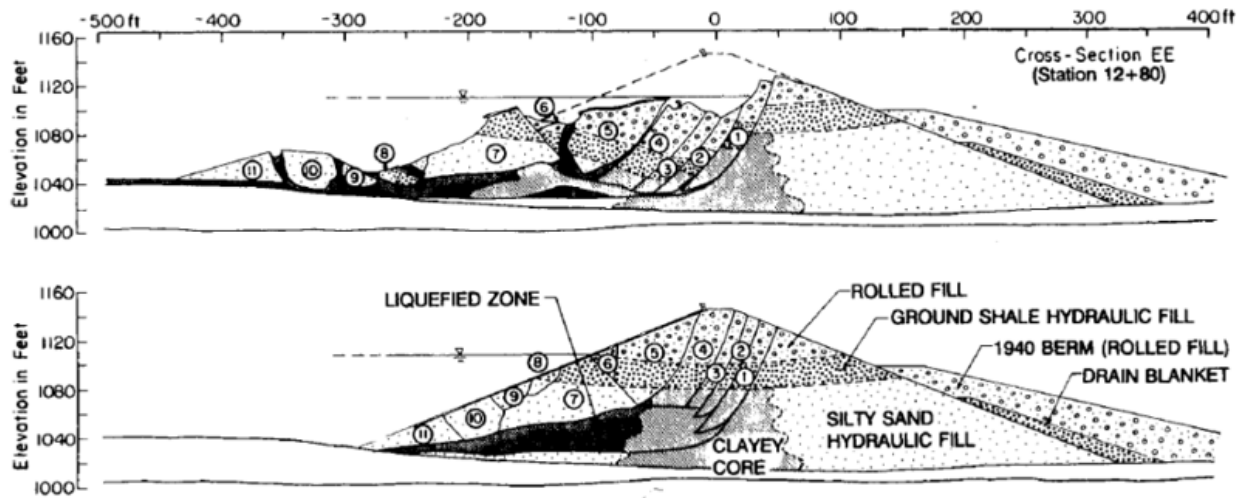


Figure A.2: Pre- and post-failure cross-section of the Lower San Fernando dam (Seed et al., 1989)

black shaded area in the lower figure indicates the liquefied region of the upstream hydraulic fill.

#### *La Marquesa dam*

The La Marquesa dam experienced liquefaction-induced slope failures on both its upstream and downstream sides during the 1985 Central Chilean earthquake (De Alba et al., 1988). Liquefaction within a thin, very loose silty sand layer in the foundation is considered the primary cause of the upstream failure. Displacements were more pronounced on the upstream (US) side, where partial excavation of the foundation toe steepened the slope. Measured displacements included approximately 2 m vertical movement at the crest and 11 m horizontal runout at the toe. The downstream (DS) side experienced relatively smaller, with 6.5 m of the toe runout. Figure A.3

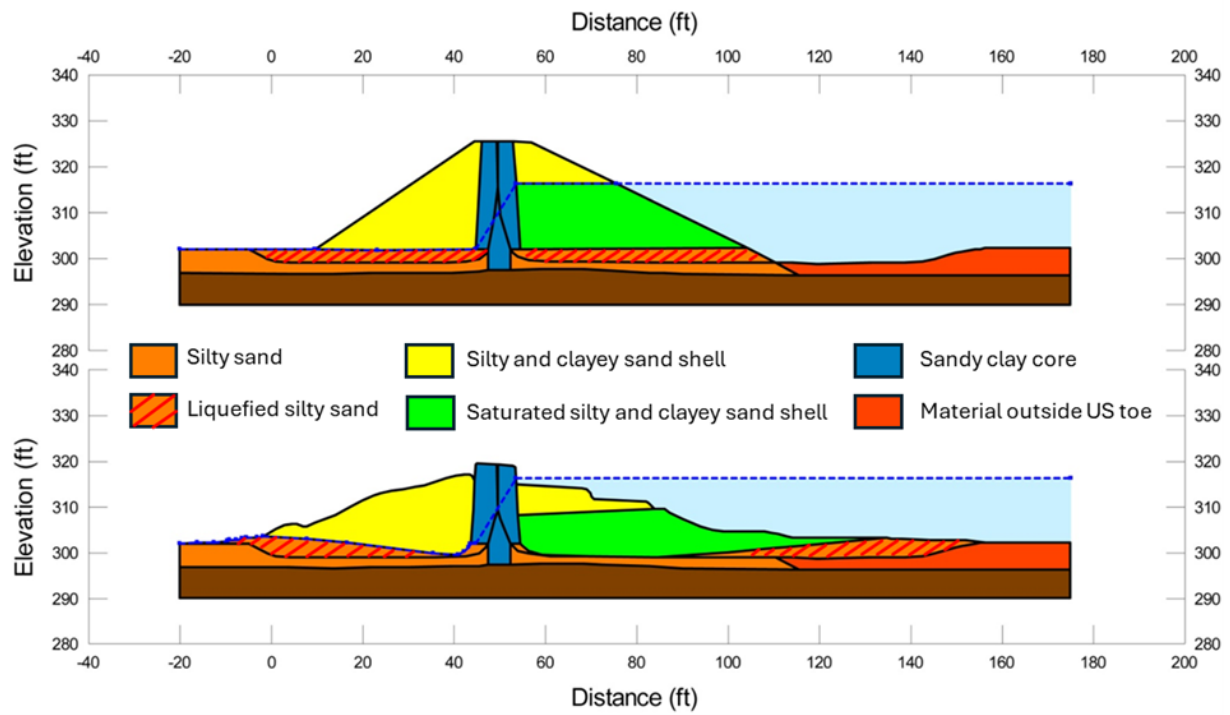


Figure A.3: Pre- and post-failure cross-section of the La Marquesa dam (modified after Weber (2015))

shows the pre- and post-failure geometry. The dam consists of a sandy clay core at the center with shells composed of silty and clayey sands.